Beamforming Design for RIS-Aided MIMO Communication: A Piece-wise Near-field Model

Weijian Chen*, Zhiqiang Wei*†‡, Zai Yang*†‡, Derrick Wing Kwan Ng§, and Michail Matthaiou¶
*School of Mathematics and Statistics, Xi'an Jiaotong University, Xi'an, Shaanxi 710049, China
†Peng Cheng Laboratory, Shenzhen, Guangdong 518055, China
‡Pazhou Laboratory (Huangpu), Guangzhou, Guangdong 510555, China
§School of Electrical Engineering and Telecommunications, University of New South Wales, Sydney, NSW 2052, Australia
¶Centre for Wireless Innovation (CWI), Queen's University Belfast, BT3 9DT Belfast, U.K.
Emails: chenwj0812@stu.xjtu.edu.cn, {yangzai, zhiqiang.wei}@xjtu.edu.cn, w.k.ng@unsw.edu.au, m.matthaiou@qub.ac.uk

***Abstract*—This work proposes a joint active and passive beamforming design for reconfigurable intelligent surface (RIS)-aided wireless communication systems. We adopt a piece-wise near-field channel model that leverages the benefits of the traditional near-field approach while enhancing its robustness against channel estimation errors (CEEs). We analyze the impact of different channel models, including the existing near-field, the proposed piece-wise near-field, and far-field channel models, on the interference distribution caused by CEEs and model mismatches. Then, by considering the interference as noise, we formulate a joint active and passive beamforming design problem to maximize the spectral efficiency (SE) and address it exploiting a block coordinate descent (BCD) framework. Simulation results demonstrate that adopting the piece-wise near-field channel model leads to an improved SE compared to both the traditional near-field and far-field models in the presence of CEEs. Additionally, the proposed piece-wise channel model strikes an effective balance between modeling accuracy and system degrees of freedom (DoF).**

***Index Terms*—Beamforming design, near-field, piece-wise near-field, reconfigurable intelligent surface.**

I. Introduction

RIS-aided wireless communications have attracted significant interest due to their excellent ability to mitigate propagation path loss through passive beamforming and to circumvent potential obstacles via establishing alternative propagation paths [1]. An RIS is a metalic planar array consisting of numerous passive elements that can be independently reconfigured. By customizing the phase shift of each RIS element based on the channel conditions, the received signal strength at the desired user can be enhanced, while undesired interference from other users can be efficiently suppressed [2], [3]. For instance, Yu *et al.* [4] proposed two efficient algorithms for point-to-point (P2P) multiple-input single-output (MISO) systems. Also, Zhang *et al.* [5] explored the joint optimization of the active and passive beamforming in RIS-aided P2P multiple-input multiple-output (MIMO) communication systems. Furthermore, Pan *et al.* [6] aimed to maximize the weighted sum rate of users in multi-cell scenarios, while Wei *et al.* [7] explored RISs in unmanned aerial vehicle-based communication systems. It is worth noting that these studies assumed a far-field channel model, which is only applicable when the RIS is positioned far from both the transmitter (Tx) and the users.

The work of M. Matthaiou was supported by the European Research Council (ERC) under the European Unions Horizon 2020 research and innovation programme (grant agreement No. 101001331).

In practice, the electromagnetic (EM) radiation field can be divided into two regions: the far-field and the near-field. The demarcation between these zones is determined by the Rayleigh distance, which is proportional to the square of the array aperture and is inversely proportional to the signal carrier wavelength [8]. Specially, in the far-field region, EM field propagation is typically modeled by planar waves with a certain approximation error, while in the near-field region, propagation is accurately modeled by spherical waves. In fact, with emerging high-frequency communications, utilizing large-aperture antenna arrays for potential power gains can also increase the Rayleigh distance up to a hundred meters, such that the far-field assumptions are no longer hold.

In fact, adopting a near-field channel model for designing RIS-aided wireless communication systems is appropriate. Firstly, deploying an RIS close to the Tx or user enhances its performance gain, indicating the suitability of a near-field channel model. Secondly, this proximity requires modeling the channel with spherical waves, which can potentially increases the system design DoF. However, near-field communications also pose various technical challenges, such as complex channel characterization and heightened sensitivity to CEEs, requiring precise beam focusing to maintain a satisfactory performance [8].

This work presents a joint active and passive beamforming design for RIS-aided MIMO wireless communication systems adopting a piece-wise near-field channel model. In particular, we analyze the covariance matrices of the interference distribution caused by CEEs and model mismatches for different channel models, demonstrating the benefits of exploiting the piece-wise near-field channel model. A BCD approach is adopted to alternatively optimize the active and passive beamforming strategies, while the alternating direction penalty method (ADPM) is leveraged to address the constant modulus constraint on the RIS reflection coefficients. Simulation results demonstrate the DoF gain and enhanced robustness of provided by the piece-wise near-filed channel model compared to the far-field and traditional near-field models.

Notations: $\mathbb{C}$ denotes the set of complex numbers. $\Re$ extracts the real part of a complex number. For matrix $\boldsymbol{A}$, $\mathbb{E}\{\boldsymbol{A}\}$, $\boldsymbol{A}^T$, $\boldsymbol{A}^H$, $\|\boldsymbol{A}\|_F$, $\boldsymbol{A}^{-1}$, rank $(\boldsymbol{A})$, and tr $(\boldsymbol{A})$ denote the expectation, matrix transpose, conjugate transpose, Frobenius norm, inverse, rank, and trace of $\boldsymbol{A}$, respectively; $[\boldsymbol{A}]_{ij}$ extracts the (i,j)-th

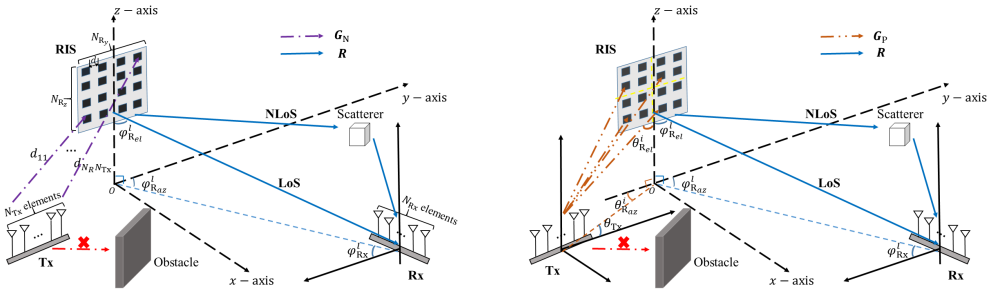

(a) Near-field model for the Tx-RIS channel.

(b) Piece-wise near-field model for the Tx-RIS channel.

Fig. 1. The considered RIS-aided P2P wireless communication system.

element of matrix $\boldsymbol{A}$. $\mathrm{diag}(\mathbf{x})$ is a diagonal matrix with its main diagonal entries given by $\mathbf{x}$. $\mathcal{CN}(\boldsymbol{\mu}, \boldsymbol{\Sigma})$ denotes a circularly symmetric complex Gaussian random vector distribution with mean $\boldsymbol{\mu}$ and covariance matrix $\boldsymbol{\Sigma}$. The symbols $\otimes$ and $\circ$ represent the Kronecker and Hadamard products, respectively. The symbol $\angle$ represents the phase of a complex number.

II. System Model

A. System Model

We consider a RIS-aided point-to-point (P2P) MIMO wireless communication system, as illustrated in Fig. 1, where the RIS is deployed close to a Tx to assist the data transmission from the Tx to a receiver (Rx). The Tx is equipped with N_{Tx} antennas and sends N_{s} ($\leq N_{\mathrm{Tx}}$) independent data streams to the Rx, which has N_{Rx} antennas. Besides, the RIS comprises $N_{\mathrm{R}} = N_{\mathrm{R}_y} \times N_{\mathrm{R}_z}$ passive elements. We assume that there is no direct link from the Tx to the Rx due to blockages [9]. Furthermore, the narrowband channels from the Tx to the RIS and from the RIS to the Rx are denoted by $\boldsymbol{G} \in \mathbb{C}^{N_{\mathrm{R}} \times N_{\mathrm{Tx}}}$ and $\boldsymbol{R} \in \mathbb{C}^{N_{\mathrm{Rx}} \times N_{\mathrm{R}}}$, respectively. The phase shift matrix of the RIS is denoted by $\boldsymbol{\Phi} = \mathrm{diag}(\phi_1, \phi_2, ..., \phi_{N_{\mathrm{R}}}) \in \mathbb{C}^{N_{\mathrm{R}} \times N_{\mathrm{R}}}$, to perform passive beamforming, where $\phi_{n_{\mathrm{R}}} = e^{j\zeta_{n_{\mathrm{R}}}}$ and $\zeta_{n_{\mathrm{R}}} \in [0, 2\pi]$ is the phase shift introduced by the n_{R}-th RIS element, $\forall n_{\mathrm{R}} \in \{1, \ldots, N_{\mathrm{R}}\}$. We denote the symbols transmitted from the Tx to the Rx as $\boldsymbol{s} \in \mathbb{C}^{N_{\mathrm{s}} \times 1} \sim \mathcal{CN}(\mathbf{0}, \mathbf{I}_{N_{\mathrm{s}}})$. The received signal $\boldsymbol{y} \in \mathbb{C}^{N_{\mathrm{Rx}} \times 1}$ at the Rx is given by

$$\boldsymbol{y} = \boldsymbol{R}\boldsymbol{\Phi}\boldsymbol{G}\boldsymbol{W}\boldsymbol{s} + \boldsymbol{n} = \boldsymbol{H}\boldsymbol{W}\boldsymbol{s} + \boldsymbol{n}, \tag{1}$$

where $\boldsymbol{W} \in \mathbb{C}^{N_{\mathrm{Tx}} \times N_{\mathrm{s}}}$ is the active beamforming matrix at the Tx and $\boldsymbol{n} \in \mathbb{C}^{N_{\mathrm{Rx}} \times 1} \sim \mathcal{CN}(\mathbf{0}, \sigma^2 \mathbf{I}_{N_{\mathrm{Rx}}})$ is the additive white Gaussian noise (AWGN) at the Rx with noise power σ^2. For the sake of presentation, we define the cascaded channel between the Tx and Rx as $\boldsymbol{H} = \boldsymbol{R}\boldsymbol{\Phi}\boldsymbol{G}$.

B. Channel Models

We consider a near-field channel model for the Tx-RIS link and a far-field multi-path channel model for the RIS-Rx link which is illustrated in Fig. 1(a). To avoid confusion, we adopt different channel models, i.e., $\boldsymbol{G}_{\mathrm{N}}, \boldsymbol{G}_{\mathrm{P}}$, and $\boldsymbol{G}_{\mathrm{F}}$, to represent the link between Tx-RIS. In particular, assuming a line-of-sight (LoS)-dominated propagation between the Tx and RIS, the corresponding Tx-RIS channel is modeled as [10]

$$[\boldsymbol{G}_{\mathrm{N}}]_{n_{\mathrm{R}} n_{\mathrm{Tx}}} = \alpha_{n_{\mathrm{R}} n_{\mathrm{Tx}}} e^{-j\frac{2\pi}{\lambda} d_{n_{\mathrm{R}} n_{\mathrm{Tx}}}}, \tag{2}$$

where $\alpha_{n_{\mathrm{R}} n_{\mathrm{Tx}}} = \frac{\lambda^2}{(4\pi d_{n_{\mathrm{R}} n_{\mathrm{Tx}}})^2}$ is the associated path coefficient, λ is wavelength, and $d_{n_{\mathrm{R}} n_{\mathrm{Tx}}}$ is the distance between the n_{Tx}-th antenna of the Tx and the n_{R}-th element of the RIS. In contrast, the Tx-RIS channel is approximated by a far-field channel model in the literature [11], i.e.,

$$\boldsymbol{G}_{\mathrm{F}} = \gamma \boldsymbol{a}_{N_{\mathrm{R}}}(\psi_{\mathrm{R}_{\mathrm{az}}}, \psi_{\mathrm{R}_{\mathrm{el}}}) \boldsymbol{a}_{N_{\mathrm{Tx}}}^H(\theta_{\mathrm{Tx}}), \tag{3}$$

where $\gamma = \frac{\lambda^2}{(4\pi d_{\mathrm{TR}})^2} e^{-j\frac{2\pi}{\lambda} d_{\mathrm{TR}}}$ is the path coefficient and d_{TR} is the distance between the centers of Tx and RIS. Moreover, $\boldsymbol{a}_{N_{\mathrm{Tx}}}(\theta_{\mathrm{Tx}}) \in \mathbb{C}^{N_{\mathrm{Tx}} \times 1}$ and $\boldsymbol{a}_{N_{\mathrm{R}}}(\psi_{\mathrm{R}_{\mathrm{az}}}, \psi_{\mathrm{R}_{\mathrm{el}}}) \in \mathbb{C}^{N_{\mathrm{R}} \times 1}$ are the array response vectors at the Tx and RIS respectively, which are given by

$$\boldsymbol{a}_{N_{\mathrm{Tx}}}(\theta_{\mathrm{Tx}}) = \left[1, \cdots, e^{-j\frac{2\pi}{\lambda}(N_{\mathrm{Tx}}-1)d\sin\theta_{\mathrm{Tx}}}\right]^T, \tag{4}$$

$$\boldsymbol{a}_{N_{\mathrm{R}}}(\psi_{\mathrm{R}_{\mathrm{az}}}, \psi_{\mathrm{R}_{\mathrm{el}}}) = \left[1, \cdots, e^{-j\frac{2\pi}{\lambda}(N_{\mathrm{R}_y}-1)d\sin\psi_{\mathrm{R}_{\mathrm{az}}}\cos\psi_{\mathrm{R}_{\mathrm{el}}}}\right]^T \otimes \left[1, \cdots, e^{-j\frac{2\pi}{\lambda}(N_{\mathrm{R}_z}-1)d\sin\psi_{\mathrm{R}_{\mathrm{az}}}\sin\psi_{\mathrm{R}_{\mathrm{el}}}}\right]^T, \tag{5}$$

respectively, where θ_{Tx} is the azimuth angle of departure (AoD) from the Tx to the center of the RIS, while $\psi_{\mathrm{R}_{\mathrm{az}}}, \psi_{\mathrm{R}_{\mathrm{el}}}$ are the azimuth and elevation angles of arrival (AoAs) at the center of the RIS, respectively.

On the other hand, based on the Saleh-Valenzuela channel model [12], the RIS-Rx channel matrix is given by

$$\boldsymbol{R} = \textstyle\sum_{l=1}^{L_{\mathrm{Rx}}} \beta_l \boldsymbol{a}_{N_{\mathrm{Rx}}}(\varphi_{\mathrm{Rx}}^l) \boldsymbol{a}_{N_{\mathrm{R}}}^H(\varphi_{\mathrm{R}_{\mathrm{az}}}^l, \varphi_{\mathrm{R}_{\mathrm{el}}}^l), \tag{6}$$

where $\beta_l = \frac{\lambda^2}{(4\pi d_{\mathrm{RR}})^2} e^{-j\frac{2\pi}{\lambda} d_{\mathrm{RR}}}$ is the path coefficient of the l-th path between the RIS and Rx, d_{RR} is the distance between the centers of RIS and Rx, and L_{Rx} is the total number of paths. The vectors $\boldsymbol{a}_{N_{\mathrm{Rx}}}(\varphi_{\mathrm{Rx}}^l) \in \mathbb{C}^{N_{\mathrm{Rx}} \times 1}$ and $\boldsymbol{a}_{N_{\mathrm{R}}}(\varphi_{\mathrm{R}_{\mathrm{az}}}^l, \varphi_{\mathrm{R}_{\mathrm{el}}}^l) \in \mathbb{C}^{N_{\mathrm{R}} \times 1}$ are defined similar to $\boldsymbol{a}_{N_{\mathrm{Tx}}}(\theta_{\mathrm{Tx}})$ and $\boldsymbol{a}_{N_{\mathrm{R}}}(\psi_{\mathrm{R}_{\mathrm{az}}}, \psi_{\mathrm{R}_{\mathrm{el}}})$, respectively, and they represent the array response vectors at the Rx and the RIS, respectively. Here, φ_{Rx}^l is the azimuth AoA of the l-th path at the Rx, while $\varphi_{\mathrm{R}_{\mathrm{az}}}^l$ and $\varphi_{\mathrm{R}_{\mathrm{el}}}^l$ are the azimuth and elevation AoDs of the l-th path from the RIS to the Rx, respectively.

Note that for the near-field channel model in (2), beam-focusing is required for passive beamforming design at the RIS, which is more sensitive to CEEs than conventional beam steering for the far-field channel model. Therefore, we propose a piece-wise near-field channel model to approximate the near-field channel in (2). Our proposal involves equally divide the

N_{R_y} RIS elements in each row of the RIS into K subarrays, and divide the N_{R_z} RIS elements in each column of the RIS into K subarrays. Without lost of generality, we assume that both $\frac{N_{\mathrm{R}_y}}{K}$ and $\frac{N_{\mathrm{R}_z}}{K}$ are integers. As a result, the original RIS is divided into K^2 subsurfaces and the Rayleigh distance is reduced by a factor of K^2. Consequently, we can safely assume that the channel between each subsurface and the Tx follows a far-field channel model. Thus, the proposed piece-wise near-field channel matrix, $\boldsymbol{G}_{\mathrm{P}}$, is given by

$$\boldsymbol{G}_{\mathrm{P}} = \left(\begin{bmatrix} \boldsymbol{g}_1^{\mathrm{h}} \\ \vdots \\ \boldsymbol{g}_K^{\mathrm{h}} \end{bmatrix} \otimes \begin{bmatrix} \boldsymbol{g}_1^{\mathrm{v}} \\ \vdots \\ \boldsymbol{g}_K^{\mathrm{v}} \end{bmatrix} \right) \boldsymbol{a}_{N_{\mathrm{Tx}}}^H(\theta_{\mathrm{Tx}}), \tag{7}$$

where $\boldsymbol{a}_{N_{\mathrm{Tx}}}(\theta_{\mathrm{Tx}})$ was defined in (4), $\boldsymbol{g}_i^{\mathrm{h}} \in \mathbb{C}^{\frac{N_{\mathrm{R}_y}}{K} \times 1}$ and $\boldsymbol{g}_i^{\mathrm{v}} \in \mathbb{C}^{\frac{N_{\mathrm{R}_z}}{K} \times 1}$ are defined by

$$\boldsymbol{g}_i^{\mathrm{h}} = \frac{\lambda}{4\pi r_i} e^{-j\frac{\pi}{\lambda} r_i} \boldsymbol{b}_{\frac{N_{\mathrm{R}_y}}{K}}(\theta_{\mathrm{R}_{az}}^i, \theta_{\mathrm{R}_{el}}^i), i = 1, \ldots, K, \tag{8}$$

$$\boldsymbol{g}_i^{\mathrm{v}} = \frac{\lambda}{4\pi r_i} e^{-j\frac{\pi}{\lambda} r_i} \boldsymbol{b}_{\frac{N_{\mathrm{R}_z}}{K}}(\theta_{\mathrm{R}_{az}}^i, \theta_{\mathrm{R}_{el}}^i), i = 1, \ldots, K, \tag{9}$$

respectively. In (8) and (9), r_i, $\theta_{\mathrm{R}_{\mathrm{az}}}^i$ and $\theta_{\mathrm{R}_{\mathrm{el}}}^i$ are the distance, azimuth, and elevation AoAs from the Tx to the center of the i-th subsurface, respectively. The vectors $\boldsymbol{b}_{\frac{N_{\mathrm{R}_y}}{K}}(\theta_{\mathrm{R}_{\mathrm{az}}}^i, \theta_{\mathrm{R}_{\mathrm{el}}}^i)$ and $\boldsymbol{b}_{\frac{N_{\mathrm{R}_z}}{K}}(\theta_{\mathrm{R}_{\mathrm{az}}}^i, \theta_{\mathrm{R}_{\mathrm{el}}}^i)$ are the horizontal and vertical array response vectors of the i-th subsurface and they are given by

$$\boldsymbol{b}_{\frac{N_{\mathrm{R}_y}}{K}}(\theta_{\mathrm{R}_{\mathrm{az}}}^i, \theta_{\mathrm{R}_{\mathrm{el}}}^i) = \left[1, \cdots, e^{-j\frac{2\pi}{\lambda}(\frac{N_{\mathrm{R}_y}}{K}-1)d \sin\theta_{\mathrm{R}_{\mathrm{az}}}^i \cos\theta_{\mathrm{R}_{\mathrm{el}}}^i}\right]^T, \tag{10}$$

$$\boldsymbol{b}_{\frac{N_{\mathrm{R}_z}}{K}}(\theta_{\mathrm{R}_{\mathrm{az}}}^i, \theta_{\mathrm{R}_{\mathrm{el}}}^i) = \left[1, \cdots, e^{-j\frac{2\pi}{\lambda}(\frac{N_{\mathrm{R}_z}}{K}-1)d \sin\theta_{\mathrm{R}_{\mathrm{az}}}^i \sin\theta_{\mathrm{R}_{\mathrm{el}}}^i}\right]^T, \tag{11}$$

respectively. For illustration, let us take $K = 2$ as an example, which is shown in Fig. 1(b). In this case, the piece-wise near-field channel matrix $\boldsymbol{G}_{\mathrm{P}}$ is given by

$$\boldsymbol{G}_{\mathrm{P}} = \left(\begin{bmatrix} \boldsymbol{g}_1^{\mathrm{h}} \\ \boldsymbol{g}_2^{\mathrm{h}} \end{bmatrix} \otimes \begin{bmatrix} \boldsymbol{g}_1^{\mathrm{v}} \\ \boldsymbol{g}_2^{\mathrm{v}} \end{bmatrix} \right) \boldsymbol{a}_{\mathrm{Tx}}^H(\theta_{\mathrm{Tx}}). \tag{12}$$

If the number of subsurfaces is $K^2 = 1$, the piece-wise near-field channel model degenerates to the far-field case $\boldsymbol{G}_{\mathrm{F}}$ in (3). If $K = N_{\mathrm{R}_y} = N_{\mathrm{R}_z}$, the piece-wise near-field model becomes the accurate traditional near-field channel model $\boldsymbol{G}_{\mathrm{N}}$ in (2). In other words, the piece-wise near-field channel model bridges the near-field and the far-field via fine tuning the number of subsurfaces. Additionally, by availing of characteristics from the near-field channel model, the piece-wise channel matrix in (7) maintains a higher rank than the far-field channel matrix in (3), i.e., $\mathrm{rank}(\boldsymbol{G}_{\mathrm{P}}) \geq \mathrm{rank}(\boldsymbol{G}_{\mathrm{F}}) = 1$ [8]. Thus, adopting the proposed model facilitates the exploiting of system DoF for performance enhancement by leveraging distance and angle diversity among different subsurfaces and improves robustness against distance and angle errors by piece beam steering when there exist CEEs.

III. Analysis of Interference Distribution in Different Channel Models

A. Channel Estimation Error Models

Note that the actual channel between the Tx and RIS, which should follow a near-field channel model in the considered system, is composed of the estimated channel, the corresponding estimation error, and the model mismatch. In the following, we represent the channel $\boldsymbol{G}_{\mathrm{N}}$, by different channel models:

$$\boldsymbol{G}_{\mathrm{N}} = \hat{\boldsymbol{G}}_{\mathrm{N}} + \Delta\boldsymbol{G}_{\mathrm{N}} + \Delta\boldsymbol{M}_{\mathrm{N}}, \quad \text{[Conventional]} \tag{13}$$

$$\boldsymbol{G}_{\mathrm{N}} = \hat{\boldsymbol{G}}_{\mathrm{P}} + \Delta\boldsymbol{G}_{\mathrm{P}} + \Delta\boldsymbol{M}_{\mathrm{P}}, \text{and} \quad \text{[Proposed]} \tag{14}$$

$$\boldsymbol{G}_{\mathrm{N}} = \hat{\boldsymbol{G}}_{\mathrm{F}} + \Delta\boldsymbol{G}_{\mathrm{F}} + \Delta\boldsymbol{M}_{\mathrm{F}}. \quad \text{[Far-field]} \tag{15}$$

For concise notation, we adopt subscripts $\{1\} = \{\mathrm{N}\}$, $\{2\} = \{\mathrm{P}\}$, and $\{3\} = \{\mathrm{F}\}$ to denote the conventional near-field, the proposed piece-wise near-field, and the far-field channel models, respectively. Additionally, $\hat{\boldsymbol{G}}_i$, $\Delta\boldsymbol{G}_i$, and $\Delta\boldsymbol{M}_i$, where $i = 1, 2, 3$, represent the estimated channel, the CEEs, and the model mismatches of different channel models. The left-hand side of (13), (14), and (15) represents the ground-truth near-field channel matrix $\boldsymbol{G}_{\mathrm{N}}$. As shown in (2), (3), and (7), different channel models approximate $\boldsymbol{G}_{\mathrm{N}}$ with different channel matrix structures, i.e., $\boldsymbol{G}_{\mathrm{N}} = \boldsymbol{G}_i + \Delta\boldsymbol{M}_i$, where $\boldsymbol{G}_i = \hat{\boldsymbol{G}}_i + \Delta\boldsymbol{G}_i$, is the traditional channel model without considering model mismatch.

Assuming that the model mismatches are deterministic and the CEE follows a matrix-variate Gaussian distribution [13], we have

$$\boldsymbol{G}_{\mathrm{N}} = \hat{\boldsymbol{G}}_i + \Delta\boldsymbol{M}_i + \Delta\boldsymbol{G}_i, \text{ and} \tag{16}$$

$$\Delta\boldsymbol{G}_i \sim \mathcal{CN}_{N_{\mathrm{R}}, N_{\mathrm{Tx}}}(\boldsymbol{0}, \sigma_{\boldsymbol{G}_i}^2 \mathbf{I}_{N_{\mathrm{R}}} \otimes \mathbf{I}_{N_{\mathrm{Tx}}}). \tag{17}$$

where $\mathcal{CN}_{N_{\mathrm{R}}, N_{\mathrm{Tx}}}(\boldsymbol{0}, \sigma_{\boldsymbol{G}_i}^2 \mathbf{I}_{N_{\mathrm{R}}} \otimes \mathbf{I}_{N_{\mathrm{Tx}}})$ represents the matrix-variate complex Gaussian distribution with the row and column covariance matrices are $\sigma_{\boldsymbol{G}_i}^2 \mathbf{I}_{N_{\mathrm{R}}}$ and $\mathbf{I}_{N_{\mathrm{Tx}}}$, respectively. Then, the distribution of the overall CSI imperfection $\Delta\widetilde{\boldsymbol{G}}_i = \Delta\boldsymbol{G}_i + \Delta\boldsymbol{M}_i$ follows

$$\Delta\widetilde{\boldsymbol{G}}_i \sim \mathcal{CN}_{N_{\mathrm{R}}, N_{\mathrm{Tx}}}(\Delta\boldsymbol{M}_i, \sigma_{\boldsymbol{G}_i}^2 \mathbf{I}_{N_{\mathrm{R}}} \otimes \mathbf{I}_{N_{\mathrm{Tx}}}). \tag{18}$$

Similarly, the channel between the RIS and Rx is given by

$$\boldsymbol{R} = \hat{\boldsymbol{R}} + \Delta\boldsymbol{R}, \Delta\boldsymbol{R} \sim \mathcal{CN}_{N_{\mathrm{Rx}}, N_{\mathrm{R}}}(\boldsymbol{0}, \sigma_{\boldsymbol{R}}^2 \mathbf{I}_{N_{\mathrm{Rx}}} \otimes \mathbf{I}_{N_{\mathrm{R}}}), \tag{19}$$

where $\hat{\boldsymbol{R}}$ and $\Delta\boldsymbol{R}$ represent the estimated channel and CEE of the RIS-Rx channel, respectively. Since $\boldsymbol{G}$ and $\boldsymbol{R}$ represent the channel matrices for the Tx-RIS and RIS-Rx links, respectively, we assume $\Delta\widetilde{\boldsymbol{G}}_i$ and $\Delta\boldsymbol{R}$ are independent of each other to facilitate the subsequent analysis and design [14].

B. Covariance Matrix of the Interference-plus-Noise

For concise notation, let us drop the subscript for now. Assuming that the estimation of the Tx-RIS and RIS-Rx links are separately executed with their estimated values $\hat{\boldsymbol{G}}$ and $\hat{\boldsymbol{R}}$ [11], respectively, the estimated cascaded channel is given by

$$\hat{\boldsymbol{H}} = \hat{\boldsymbol{R}}\boldsymbol{\Phi}\hat{\boldsymbol{G}}. \tag{20}$$

Then, we define $\Delta\boldsymbol{H}$ and $\Delta\boldsymbol{H}_{\mathrm{M}}$ as the cascaded channel estimation error and the corresponding model mismatch error, respectively, which are given by

$$\Delta\boldsymbol{H} = \Delta\boldsymbol{R}\boldsymbol{\Phi}\hat{\boldsymbol{G}} + \hat{\boldsymbol{R}}\boldsymbol{\Phi}\Delta\boldsymbol{G} + \Delta\boldsymbol{R}\boldsymbol{\Phi}\Delta\boldsymbol{G} \text{ and} \tag{21}$$

$$\Delta\boldsymbol{H}_{\mathrm{M}} = \hat{\boldsymbol{R}}\boldsymbol{\Phi}\Delta\boldsymbol{M} + \Delta\boldsymbol{R}\boldsymbol{\Phi}\Delta\boldsymbol{M}, \tag{22}$$

respectively. The received signal at the Rx in (1) can be reformulated as

$$\boldsymbol{y} = (\hat{\boldsymbol{H}} + \Delta\boldsymbol{H} + \Delta\boldsymbol{H}_{\mathrm{M}})\boldsymbol{W}\boldsymbol{s} + \boldsymbol{n} = \hat{\boldsymbol{H}}\boldsymbol{W}\boldsymbol{s} + \hat{\boldsymbol{n}}, \tag{23}$$

with the interference-plus-noise signal $\hat{\boldsymbol{n}} = (\Delta\boldsymbol{H} + \Delta\boldsymbol{H}_{\mathrm{M}})\boldsymbol{W}\boldsymbol{s} + \boldsymbol{n}$.

For the sake of analysis, we assume that

$$\|\Delta\boldsymbol{R}\|_F \ll \|\hat{\boldsymbol{R}}\|_F, \|\Delta\boldsymbol{G}\|_F \ll \|\hat{\boldsymbol{G}}\|_F, \text{ and } \|\Delta\boldsymbol{M}\|_F \ll \|\hat{\boldsymbol{G}}\|_F, \quad (24)$$

respectively, which implies a relatively small CEE and model mismatch. By discarding the minor terms $\Delta\boldsymbol{R}\boldsymbol{\Phi}\Delta\boldsymbol{G}$ and $\Delta\boldsymbol{R}\boldsymbol{\Phi}\Delta\boldsymbol{M}$ in (21) and (22), $\Delta\boldsymbol{H}$ and $\Delta\boldsymbol{H}_{\mathrm{M}}$ can be approximated as:

$$\Delta\boldsymbol{H} \approx \Delta\boldsymbol{R}\boldsymbol{\Phi}\hat{\boldsymbol{G}} + \hat{\boldsymbol{R}}\boldsymbol{\Phi}\Delta\boldsymbol{G}, \text{ and} \quad (25)$$

$$\Delta\boldsymbol{H}_{\mathrm{M}} \approx \hat{\boldsymbol{R}}\boldsymbol{\Phi}\Delta\boldsymbol{M}, \quad (26)$$

respectively. Notice that $\Delta\boldsymbol{H}_{\mathrm{M}}$ in (26) is approximately deterministic when the passive beamforming matrix $\boldsymbol{\Phi}$ and the estimated channel $\hat{\boldsymbol{R}}$ are given. The covariance matrix of the interference-plus-noise signal $\hat{\boldsymbol{n}}$ is given by

$$\begin{aligned}\boldsymbol{\Sigma}_{\hat{\boldsymbol{n}}} &= \mathbb{E}\{\hat{\boldsymbol{n}}\hat{\boldsymbol{n}}^H\} \\ &= \Delta\boldsymbol{H}_{\mathrm{M}}\boldsymbol{W}\boldsymbol{W}^H\Delta\boldsymbol{H}_{\mathrm{M}}^H + \mathbb{E}\{\Delta\boldsymbol{R}\boldsymbol{\Phi}\hat{\boldsymbol{G}}\boldsymbol{W}\boldsymbol{W}^H\hat{\boldsymbol{G}}^H\boldsymbol{\Phi}^H\Delta\boldsymbol{R}^H\} \\ &\quad + \mathbb{E}\{\hat{\boldsymbol{R}}\boldsymbol{\Phi}\Delta\boldsymbol{G}\boldsymbol{W}\boldsymbol{W}^H\Delta\boldsymbol{G}^H\boldsymbol{\Phi}^H\hat{\boldsymbol{R}}^H\} + \sigma^2\mathbf{I}. \end{aligned} \quad (27)$$

According to the Lemma 1 in [15], for $\boldsymbol{X} \sim \mathcal{CN}_{n,m}(\hat{\boldsymbol{X}}, \boldsymbol{R}_n \otimes \boldsymbol{R}_m)$, there is $\mathbb{E}\{\boldsymbol{X}\boldsymbol{Z}\boldsymbol{X}^H\} = \hat{\boldsymbol{X}}\boldsymbol{Z}\hat{\boldsymbol{X}}^H + \mathrm{tr}(\boldsymbol{Z}\boldsymbol{R}_m^T)\boldsymbol{R}_n$, then we have

$$\mathbb{E}\left\{\Delta\boldsymbol{R}\boldsymbol{\Phi}\hat{\boldsymbol{G}}\boldsymbol{W}\boldsymbol{W}^H\hat{\boldsymbol{G}}^H\boldsymbol{\Phi}^H\Delta\boldsymbol{R}^H\right\} = \sigma_{\boldsymbol{R}}^2\mathrm{tr}(\hat{\boldsymbol{G}}\boldsymbol{W}\boldsymbol{W}^H\hat{\boldsymbol{G}}^H)\mathbf{I}, \quad (28)$$

and

$$\mathbb{E}\left\{\hat{\boldsymbol{R}}\boldsymbol{\Phi}\Delta\boldsymbol{G}\boldsymbol{W}\boldsymbol{W}^H\Delta\boldsymbol{G}^H\boldsymbol{\Phi}^H\hat{\boldsymbol{R}}^H\right\} = \sigma_{\boldsymbol{G}}^2\mathrm{tr}(\boldsymbol{W}\boldsymbol{W}^H)\hat{\boldsymbol{R}}\hat{\boldsymbol{R}}^H. \quad (29)$$

Inserting (28) and (29) into (27), the covariance matrix $\boldsymbol{\Sigma}_{\hat{\boldsymbol{n}}}$ is given by

$$\begin{aligned}\boldsymbol{\Sigma}_{\hat{\boldsymbol{n}}} &= \Delta\boldsymbol{H}_{\mathrm{M}}\boldsymbol{W}\boldsymbol{W}^H\Delta\boldsymbol{H}_{\mathrm{M}}^H + \sigma_{\boldsymbol{R}}^2\mathrm{tr}(\hat{\boldsymbol{G}}\boldsymbol{W}\boldsymbol{W}^H\hat{\boldsymbol{G}}^H)\mathbf{I} \\ &\quad + \sigma_{\boldsymbol{G}}^2\mathrm{tr}(\boldsymbol{W}\boldsymbol{W}^H)\hat{\boldsymbol{R}}\hat{\boldsymbol{R}}^H + \sigma^2\mathbf{I}. \end{aligned} \quad (30)$$

Substituting the subscript $i = \{1, 2, 3\}$, we can obtain the interference distributions $\boldsymbol{\Sigma}_{\hat{\boldsymbol{n}}}^i$ for the three channel models caused by the CEEs and model mismatches, respectively.

IV. Problem Formulation And Solution

A. Problem Formulation

The joint active and passive beamforming design is to maximize the SE under the transmit power constraint at the Tx and the constant modulus constraint for the phase control variables at the RIS, which is formulated as the following optimization problem [14]:

$$\begin{aligned}\max_{\boldsymbol{W},\boldsymbol{\Phi}} \quad & \mathcal{R}(\boldsymbol{W}, \boldsymbol{\Phi}) = \log_2\det(\mathbf{I}_{N_{\mathrm{Rx}}} + \hat{\boldsymbol{H}}\boldsymbol{W}\boldsymbol{W}^H\hat{\boldsymbol{H}}^H\boldsymbol{\Sigma}_{\hat{\boldsymbol{n}}}^{-1}) \\ \text{s.t.} \quad & \|\boldsymbol{W}\|_F^2 \le P_{\mathrm{Tx}}, \\ & |\boldsymbol{\phi}_{n_{\mathrm{R}}}| = 1,\ \forall n_{\mathrm{R}} = 1, \ldots, N_{\mathrm{R}}, \end{aligned} \quad (31)$$

where $\boldsymbol{\phi} = \mathrm{diag}(\boldsymbol{\Phi})$. Due to the severe variable coupling, the optimization problem in (31) is intractable and difficult to deal with. By introducing two auxiliary variables $\boldsymbol{Z} \in \mathbb{C}^{N_{\mathrm{Rx}} \times N_{\mathrm{s}}}$ and $\boldsymbol{\Omega} \in \mathbb{C}^{N_{\mathrm{s}} \times N_{\mathrm{s}}} \succeq \mathbf{0}$, the SE maximization problem in (31) is equivalently transformed to a mean square error (MSE) minimization problem as follows [16]:

$$\begin{aligned}(\mathrm{P}) \min_{\boldsymbol{W},\boldsymbol{Z},\boldsymbol{\Phi},\boldsymbol{\Omega}} \quad & \mathrm{tr}(\boldsymbol{\Omega}\boldsymbol{J}(\boldsymbol{Z}, \boldsymbol{W})) - \log\det(\boldsymbol{\Omega}) - N_{\mathrm{s}}, \\ \text{s.t.} \quad & \|\boldsymbol{W}\|_F^2 \le P_{\mathrm{Tx}}, \\ & |\boldsymbol{\phi}_{n_{\mathrm{R}}}| = 1,\ \forall n_{\mathrm{R}} = 1, \ldots, N_{\mathrm{R}}, \end{aligned} \quad (32)$$

where

$$\begin{aligned}\boldsymbol{J}(\boldsymbol{Z}, \boldsymbol{W}) &= \mathbb{E}\{(\boldsymbol{Z}^H\boldsymbol{y} - \boldsymbol{s})(\boldsymbol{Z}^H\boldsymbol{y} - \boldsymbol{s})^H\} \\ &= \boldsymbol{Z}^H(\hat{\boldsymbol{H}}\boldsymbol{W}\boldsymbol{W}^H\hat{\boldsymbol{H}}^H + \boldsymbol{\Sigma}_{\hat{\boldsymbol{n}}})\boldsymbol{Z} - \boldsymbol{Z}^H\hat{\boldsymbol{H}}\boldsymbol{W} \\ &\quad - \boldsymbol{W}^H\hat{\boldsymbol{H}}^H\boldsymbol{Z} + \mathbf{I} \end{aligned} \quad (33)$$

is the MSE matrix function. The equivalence between the SE maximization problem in (31) and the MSE minimization problem in (32) is proven similarly to [16].

B. Solution

In the following, we introduce an iterative BCD approach to acquire an effective solution to (32). The proposed approach divides (32) into three subproblems that address different variables.

1) Update the Auxiliary Variables Matrices $\boldsymbol{Z}$ and $\boldsymbol{\Omega}$: It is worth noting that when $\boldsymbol{W}$ and $\boldsymbol{\Phi}$ are given at each iteration, the optimal auxiliary variables $\boldsymbol{Z}^\star$ and $\boldsymbol{\Omega}^\star$ to minimize the objective function in (32) are respectively given by

$$\boldsymbol{Z}^\star = (\hat{\boldsymbol{H}}\boldsymbol{W}\boldsymbol{W}^H\hat{\boldsymbol{H}}^H + \boldsymbol{\Sigma}_{\hat{\boldsymbol{n}}})^{-1}\hat{\boldsymbol{H}}\boldsymbol{W} \text{ and } \boldsymbol{\Omega}^\star = (\boldsymbol{J}(\boldsymbol{Z}, \boldsymbol{W}))^{-1}. \quad (34)$$

2) Update the Active Beamforming Matrix $\boldsymbol{W}$: For given $\boldsymbol{Z}$, $\boldsymbol{\Omega}$, and $\boldsymbol{\Phi}$, the precoding matrix $\boldsymbol{W}$ can be updated by solving the following problem:

$$\begin{aligned}\min_{\boldsymbol{W}} \quad & \mathrm{tr}(\boldsymbol{\Omega}(\mathbf{I} - \boldsymbol{Z}^H\hat{\boldsymbol{H}}\boldsymbol{W})(\mathbf{I} - \boldsymbol{Z}^H\hat{\boldsymbol{H}}\boldsymbol{W})^H) + \mathrm{tr}(\boldsymbol{\Omega}\boldsymbol{Z}^H\boldsymbol{\Sigma}_{\hat{\boldsymbol{n}}}\boldsymbol{Z}) \\ \text{s.t.} \quad & \|\boldsymbol{W}\|_F^2 \le P_{\mathrm{Tx}}, \end{aligned} \quad (35)$$

which is a convex optimization problem. Adopting the Lagrangian multiplier approach [6], the optimal active beamformer at the Tx is given by

$$\begin{aligned}\boldsymbol{W}^\star = [&\hat{\boldsymbol{H}}^H\boldsymbol{Z}\boldsymbol{\Omega}\boldsymbol{Z}^H\hat{\boldsymbol{H}} + \sigma_{\boldsymbol{R}}^2\mathrm{tr}(\boldsymbol{\Omega}\boldsymbol{Z}^H\boldsymbol{Z})\hat{\boldsymbol{G}}^H\hat{\boldsymbol{G}} \\ &+ \sigma_{\boldsymbol{G}}^2\mathrm{tr}(\boldsymbol{\Omega}\boldsymbol{Z}^H\hat{\boldsymbol{R}}\hat{\boldsymbol{R}}^H\boldsymbol{Z})\mathbf{I} + N_{\mathrm{R}}\sigma_{\boldsymbol{G}}^2\sigma_{\boldsymbol{R}}^2\mathrm{tr}(\boldsymbol{\Omega}\boldsymbol{Z}^H\boldsymbol{Z})\mathbf{I} \\ &+ \eta\mathbf{I}]^{-1}\hat{\boldsymbol{H}}^H\boldsymbol{Z}\boldsymbol{\Omega}, \end{aligned} \quad (36)$$

where the optimal Lagrangian multiplier $\eta \ge 0$ can be found by the algorithm in [6]. Note that to maximize the achievable SE, we have $\|\boldsymbol{W}\|_F^2 = P_{\mathrm{Tx}}$ at the optimum [6].

3) Update the Passive Beamforming Matrix $\boldsymbol{\Phi}$: For given $\boldsymbol{Z}$, $\boldsymbol{\Omega}$, and $\boldsymbol{W}$, the passive beamforming design problem is formulated as

$$\begin{aligned}\min_{\boldsymbol{\Phi}} f(\boldsymbol{\Phi}) = &\ \mathrm{tr}(\boldsymbol{\Omega}(\mathbf{I} - \boldsymbol{Z}^H\hat{\boldsymbol{H}}\boldsymbol{W})(\mathbf{I} - \boldsymbol{Z}^H\hat{\boldsymbol{H}}\boldsymbol{W})^H) \\ &+ \ \mathrm{tr}(\boldsymbol{\Omega}\boldsymbol{Z}^H\boldsymbol{\Sigma}_{\hat{\boldsymbol{n}}}\boldsymbol{Z}) \\ \text{s.t.} \quad & |\boldsymbol{\phi}_{n_{\mathrm{R}}}| = 1,\ \forall n_{\mathrm{R}} = 1, \ldots, N_{\mathrm{R}}. \end{aligned} \quad (37)$$

Substituting $\hat{\boldsymbol{H}}$ into (37) and ignoring items that are not related to $\boldsymbol{\Phi}$, then according to [13, Lemma 10.6], the objective function in (37) can be simplified as

$$\begin{aligned}\min_{\boldsymbol{\Phi}} \quad & f(\boldsymbol{\phi}) = \boldsymbol{\phi}^H\boldsymbol{A}\boldsymbol{\phi} - 2\Re\{\boldsymbol{d}^T\boldsymbol{\phi}\} \\ \text{s.t.} \quad & |\boldsymbol{\phi}_{n_{\mathrm{R}}}| = 1,\ \forall n_{\mathrm{R}} = 1, \ldots, N_{\mathrm{R}}, \end{aligned} \quad (38)$$

where

$$\boldsymbol{A} = (\hat{\boldsymbol{R}}^H \boldsymbol{Z}\boldsymbol{\Omega}\boldsymbol{Z}^H \hat{\boldsymbol{R}}) \circ (\hat{\boldsymbol{G}}\boldsymbol{W}\boldsymbol{W}^H \hat{\boldsymbol{G}}^H)^T, \tag{39}$$

$$\boldsymbol{d} = (\boldsymbol{D}_{1,1}, \ldots, \boldsymbol{D}_{N_\mathrm{R},N_\mathrm{R}})^T \text{ and } \boldsymbol{D} = \hat{\boldsymbol{G}}\boldsymbol{W}\boldsymbol{\Omega}\boldsymbol{Z}^H \hat{\boldsymbol{R}}. \tag{40}$$

More specifically, by introducing an auxiliary variable $\boldsymbol{\phi}_0 = (e^{j\vartheta_1}, \ldots, e^{j\vartheta_{N_\mathrm{R}}}) \in \mathbb{C}^{N_\mathrm{R}\times 1}$, we equivalently recast the problem in (38) as

$$\begin{aligned} &\min_{\boldsymbol{\phi},\boldsymbol{\phi}_0} \ \boldsymbol{\phi}^H \boldsymbol{A}\boldsymbol{\phi} - 2\Re\{\boldsymbol{d}^T\boldsymbol{\phi}\} \\ &\text{s.t. } \boldsymbol{\phi} = \boldsymbol{\phi}_0, \\ &\quad |\boldsymbol{\phi}_{0_{n_\mathrm{R}}}| = 1, \ \vartheta_{n_\mathrm{R}} \in [0, 2\pi], \ \forall n_\mathrm{R} = 1, \ldots, N_\mathrm{R}. \end{aligned} \tag{41}$$

The augmented Lagrangian function of (41) is given by

$$\mathcal{L} = f(\boldsymbol{\phi}) + \Re\{\boldsymbol{u}^H(\boldsymbol{\phi} - \boldsymbol{\phi}_0)\} + \frac{\rho}{2}||\boldsymbol{\phi} - \boldsymbol{\phi}_0||_2^2, \tag{42}$$

where $f(\boldsymbol{\phi}) = \boldsymbol{\phi}^H \boldsymbol{A}\boldsymbol{\phi} - 2\Re\{\boldsymbol{d}^T\boldsymbol{\phi}\}$, while $\boldsymbol{u} \in \mathbb{C}^{N_\mathrm{R}\times 1}$ and $\rho > 0$ are the multiplier vector and the penalty factor, respectively. Next, we adopt an ADPM algorithm [17] that increases the penalty factor ρ with the evolvement of iterations to force the penalty term approaching zero to design the phase of the RIS.

When we consider the update of $\boldsymbol{\phi}_0$ in the t-th iteration of ADPM, we omit the constant terms in $\mathcal{L}$ that are irrelevant to $\boldsymbol{\phi}_0$, and the optimization problem is given by

$$\begin{aligned} &\min_{\boldsymbol{\phi}_0} \ \Re\{(-\boldsymbol{u}^{(t-1)} - \rho^{(t-1)}\boldsymbol{\phi}^{(t-1)})^H \boldsymbol{\phi}_0\} \\ &\text{s.t. } |\boldsymbol{\phi}_0| = 1, \ \vartheta_{n_\mathrm{R}} \in [0, 2\pi], \ n_\mathrm{R} = 1, \ldots, N_\mathrm{R}. \end{aligned} \tag{43}$$

The optimal solution of problem (43) is given as

$$\vartheta_{n_\mathrm{R}} = \angle\{\boldsymbol{\gamma}_{n_\mathrm{R}}^{(t-1)}\}, \tag{44}$$

where $\boldsymbol{\gamma}^{(t-1)} = \boldsymbol{u}^{(t-1)} + \rho^{(t-1)}\boldsymbol{\phi}^{(t-1)} \in \mathbb{C}^{N_\mathrm{R}\times 1}$.

When we consider the update of $\boldsymbol{\phi}$, the minimization problem is given by

$$\min_{\boldsymbol{\phi}} f(\boldsymbol{\phi}) + \Re\{(\boldsymbol{u}^{(t-1)} - \rho^{(t-1)}\boldsymbol{\phi}_0^{(t)})^H \boldsymbol{\phi}\}. \tag{45}$$

We can obtain the closed-form optimal solution to the problem in (45) as

$$\boldsymbol{\phi}^{(t)} = (2\boldsymbol{A} + \rho^{(t-1)}\mathbf{I})^{-1}(\rho^{(t-1)}\boldsymbol{\phi}_0^{(t)} - \boldsymbol{u}^{(t-1)} + 2\boldsymbol{d}). \tag{46}$$

The update rules for ρ and $\boldsymbol{u}$ are identical to those in [17].

To sum up, we provide the detailed description of the overall BCD algorithm for solving (32) in Algorithm 1. Note that the proposed problem formulation and algorithmic solution are applicable for all the three channel models in (2), (3), and (7). However, the impact of channel models on the system performance is characterized by the covariance matrices $\boldsymbol{\Sigma}_{\hat{\boldsymbol{n}}}^i$ in (31). A further extension of this work is to leverage matrix structures of different channel models to design specific algorithms aimed at exploring the impact of channel models on the system performance.

V. Numerical Results

We consider that the Tx is equipped with $N_\mathrm{Tx} = 64$ transmit antennas serving one mobile equipment equipped with $N_\mathrm{Rx} = 8$ receive antennas with the assistance of an RIS. The number of reflection elements is $N_\mathrm{R} = 256$. The path loss model utilized is a model tailored for RIS-aided near-field communication,

Algorithm 1 Overall BCD Algorithm for Addressing (32)

1: **Initialize:** $\boldsymbol{\Phi}^0$, $\boldsymbol{W}^0$, $\boldsymbol{Z}^0$ and $\boldsymbol{\Omega}^0$, tolerance accuracy ε, maximum number of iterations $r_{\max}$, the objective function value of problem (32) $P(\boldsymbol{\Phi}^0, \boldsymbol{W}^0)$.
2: **repeat**
3: Given $\boldsymbol{W}^r, \boldsymbol{\Phi}^r$, compute the auxiliary variables $\boldsymbol{Z}^r$ and $\boldsymbol{\Omega}^r$ by (34).
4: Given $\boldsymbol{Z}^r$, $\boldsymbol{\Omega}^r$ and $\boldsymbol{\Phi}^r$, determine η and compute $\boldsymbol{W}^{r+1}$ by (36).
5: Given $\boldsymbol{Z}^r$, $\boldsymbol{\Omega}^r$ and $\boldsymbol{W}^{r+1}$, compute $\boldsymbol{A}$ and $\boldsymbol{d}$ by (39).
6: Update $\boldsymbol{\phi}^{r+1}$ by alternately iterating (44) and (46), and then reconstruct $\boldsymbol{\Phi}^{r+1}$.
7: Set $r = r + 1$.
8: **until** $r > r_{\max}$ or $|P(\boldsymbol{W}^{r+1}, \boldsymbol{\Phi}^{r+1}) - P(\boldsymbol{W}^r, \boldsymbol{\Phi}^r)| < \varepsilon$
9: **Output:** $\boldsymbol{\Phi}^*, \boldsymbol{W}^*$.

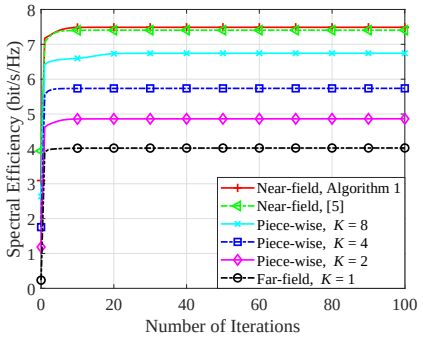

Fig. 2. Convergence behavior when $d_\mathrm{BR} = 20$ m and SNR = 10 dB.

as detailed in [10]. The carrier frequency is 30 GHz and the number of Monte Carlo experiments is 50. We assume an identical normalized CEE for the different channel models, i.e., $\sigma_{\boldsymbol{G}_i}^2 = \tau_i \cdot \mathbb{E}\{\|\boldsymbol{G}_\mathrm{N} - \Delta\boldsymbol{M}_i\|_F^2\}$ where τ_i is the normalized CEE for Tx-RIS link and it is given by

$$\tau_i = \frac{\mathbb{E}\{||\boldsymbol{G}_\mathrm{N} - \Delta\boldsymbol{M}_i - \hat{\boldsymbol{G}}_i||_F^2\}}{\mathbb{E}\{||\boldsymbol{G}_\mathrm{N} - \Delta\boldsymbol{M}_i||_F^2\}}, \ i = 1, 2, 3, \tag{47}$$

and similarly, we can define the normalized CEE $\tau_{\boldsymbol{R}}$ for the RIS-Rx link which is given by

$$\tau_{\boldsymbol{R}} = \frac{\mathbb{E}\{||\Delta\boldsymbol{R}||_F^2\}}{\mathbb{E}\{||\boldsymbol{R}||_F^2\}}. \tag{48}$$

A. Convergence Validation

We show the SEs for different channel models without considering any estimation errors in Fig. 2, i.e., $\tau_i = 0, i = 1, 2, 3$, which means that only model mismatch errors are considered. Here, we set the distance between the Tx and RIS as $d_\mathrm{BR} = 20$ m, and SNR = $10\log_{10}(P_\mathrm{Tx}/\sigma^2)$, where P_Tx and σ^2 are the power of signal and noise, respectively. We compare the performance of our proposed algorithm (i.e., Algorithm 1), with that of the algorithm in [5] under the near-field channel model, demonstrating the effectiveness of Algorithm 1. It can be seen that the performance of the piece-wise near-field channel model with multiple subsurface structures is indeed better than that of the far-field model, owing to the reduced model mismatch error as well as the increased DoF. Moreover, as the number of subsurfaces increases, the performance of adopting the piece-wise near-field channel model gradually approaches that of the conventional near-field channel model, which does not have any model mismatch error.

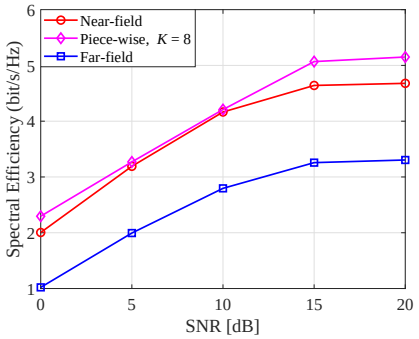

Fig. 3. The SEs versus the SNR when $\tau = 0.2$.

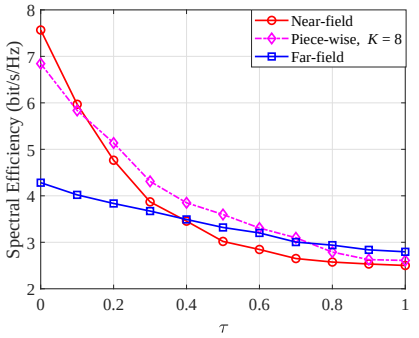

Fig. 4. The SEs versus the CEE variance when $K = 8$.

B. SE vs SNR for Different Channel Models in the Presence of CEE

Fig. 3 illustrates the SEs for different channel models at different SNR levels in the presence of CEEs with $\tau = 0.2$. The slope of each curve represents the multiplexing gain with a steeper model indicating more available DoF. The results demonstrate that the proposed piece-wise near-field channel offers greater DoF compared to the conventional far-field channel, potentially leading to an increased SE. However, owing to the beamfocusing designed based on the near-field channel model is sensitive to CEEs, adopting the piece-wise channel model can yield an even higher SE than that of the near-field channel. This is because beam steering is robust to the angle and distance, and it exploits more DoF brought by the conventional near-field channel model. Besides, we note that the achievable SEs for all the three channel models are saturated in the high SNR regime due to the presence of CEEs and potential model mismatches.

C. SE vs Normalized CEEs for Different Channel Models

In Fig. 4, the SEs for different channel models are presented under different normalized CEEs. When the normalized CEE τ is 0, we end up with the scenario without any estimation error in Fig. 2. It is observed that when the normalized CEE $\tau > 0.13$, the proposed piece-wise near-field model outperforms the near-field model due to the enhanced robustness inherited from the far-field model. Combining the results from Fig. 3 and Fig. 4, it becomes evident that the piece-wise channel model not only exceeds the DoF associated with the far-field model but also enhances the system robustness against CEEs compared to the conventional near-field model.

VI. Conclusions

This paper proposed a piece-wise near-field channel model for RIS-aided MIMO systems under CEEs. We considered three channel models (near-field, piece-wise near-field, and far-field) and analyzed their impacts on the interference distributions due to CEEs and model mismatches. By treating the interference as noise, we formulated a joint active and passive beamforming optimization to maximize SE, considering the transmit power and constant modulus constraints. The joint beamforming optimization problem was transformed into an MSE minimization problem and handled by capitalizing on the proposed algorithm. Our results showed that the piece-wise near-field model improves the DoF gain and robustness against CEEs, leading to higher SE compared to other models.

References

[1] M. Matthaiou, O. Yurduseven, H. Q. Ngo, D. Morales-Jimenez, S. L. Cotton, and V. F. Fusco, "The road to 6G: Ten physical layer challenges for communications engineers," *IEEE Commun. Mag.*, vol. 59, no. 1, pp. 64–69, Jan. 2021.

[2] T. J. Cui, M. Q. Qi, X. Wan, J. Zhao, and Q. Cheng, "Coding metamaterials, digital metamaterials and programmable metamaterials," *Light Sci. Appl.*, vol. 3, no. 10, pp. e218–e218, Oct. 2014.

[3] J. Zhang, E. Björnson, M. Matthaiou, D. W. K. Ng, H. Yang, and D. J. Love, "Prospective multiple antenna technologies for beyond 5G," *IEEE J. Sel. Areas in Commun.*, vol. 38, no. 8, pp. 1637–1660, 2020.

[4] X. Yu, D. Xu, and R. Schober, "MISO wireless communication systems via intelligent reflecting surfaces," in *Proc. IEEE ICCC*, Aug. 2019, pp. 735–740.

[5] S. Zhang and R. Zhang, "Capacity characterization for intelligent reflecting surface aided MIMO communication," *IEEE J. Sel. Areas Commun.*, vol. 38, no. 8, pp. 1823–1838, Aug. 2020.

[6] C. Pan, H. Ren, K. Wang, W. Xu, M. Elkashlan, A. Nallanathan, and L. Hanzo, "Multicell MIMO communications relying on intelligent reflecting surfaces," *IEEE Trans. Wireless Commun.*, vol. 19, no. 8, pp. 5218–5233, Aug. 2020.

[7] Z. Wei, Y. Cai, Z. Sun, D. W. K. Ng, J. Yuan, M. Zhou, and L. Sun, "Sum-rate maximization for IRS-assisted UAV OFDMA communication systems," *IEEE Trans. Wireless Commun.*, vol. 20, no. 4, pp. 2530–2550, Dec. 2020.

[8] M. Cui, Z. Wu, Y. Lu, X. Wei, and L. Dai, "Near-field MIMO communications for 6G: Fundamentals, challenges, potentials, and future directions," *IEEE Commun. Mag.*, vol. 61, no. 1, pp. 40–46, Jan. 2022.

[9] M. Z. Siddiqi and T. Mir, "Reconfigurable intelligent surface-aided wireless communications: An overview," *Intell. and Converged Netw.*, vol. 3, no. 1, pp. 33–63, Mar. 2022.

[10] E. Björnson and L. Sanguinetti, "Power scaling laws and near-field behaviors of massive MIMO and intelligent reflecting surfaces," *IEEE Open J. Commun. Soc.*, vol. 1, pp. 1306–1324, Sept. 2020.

[11] Z. Wang, L. Liu, and S. Cui, "Channel estimation for intelligent reflecting surface assisted multiuser communications: Framework, algorithms, and analysis," *IEEE Trans. Wireless Commun.*, vol. 19, no. 10, pp. 6607–6620, Oct. 2020.

[12] O. El Ayach, S. Rajagopal, S. Abu-Surra, Z. Pi, and R. W. Heath, "Spatially sparse precoding in millimeter wave MIMO systems," *IEEE Trans. Wireless Commun.*, vol. 13, no. 3, pp. 1499–1513, Mar. 2014.

[13] X. Zhang, *Matrix Analysis and Applications*. Cambridge University Press, 2017.

[14] P. Zeng, D. Qiao, H. Qian, and Q. Wu, "Joint beamforming design for IRS aided multiuser MIMO with imperfect CSI," *IEEE Trans. on Veh. Technol.*, vol. 71, no. 10, pp. 10 729–10 743, Oct. 2022.

[15] Y. Rong, "Robust design for linear non-regenerative MIMO relays with imperfect channel state information," *IEEE Trans on Signal Process.*, vol. 59, no. 5, pp. 2455–2460, May 2011.

[16] X. Zhao, S. Lu, Q. Shi, and Z.-Q. Luo, "Rethinking WMMSE: Can its complexity scale linearly with the number of BS antennas?" *IEEE Trans. Signal Process.*, vol. 71, pp. 433–446, Feb. 2023.

[17] X. Yu, G. Cui, J. Yang, J. Li, and L. Kong, "Quadratic optimization for unimodular sequence design via an ADPM framework," *IEEE Trans. Signal Process.*, vol. 68, pp. 3619–3634, May 2020.